

Imaging of strain and lattice orientation by quick scanning X-ray microscopy combined with three-dimensional reciprocal space mapping

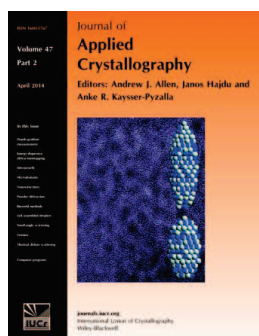
Gilbert André Chahine, Marie-Ingrid Richard, Roberto Arturo Homs-Regojo, Thu Nhi Tran-Caliste, Dina Carbone, Vincent Louis Robert Jaques, Raphael Grifone, Peter Boesecke, Jens Katzer, Ioan Costina, Hamid Djazouli, Thomas Schroeder and Tobias Urs Schüllli

J. Appl. Cryst. (2014). **47**, 762–769

Copyright © International Union of Crystallography

Author(s) of this paper may load this reprint on their own web site or institutional repository provided that this cover page is retained. Republication of this article or its storage in electronic databases other than as specified above is not permitted without prior permission in writing from the IUCr.

For further information see <http://journals.iucr.org/services/authorrights.html>



Many research topics in condensed matter research, materials science and the life sciences make use of crystallographic methods to study crystalline and non-crystalline matter with neutrons, X-rays and electrons. Articles published in the *Journal of Applied Crystallography* focus on these methods and their use in identifying structural and diffusion-controlled phase transformations, structure-property relationships, structural changes of defects, interfaces and surfaces, etc. Developments of instrumentation and crystallographic apparatus, theory and interpretation, numerical analysis and other related subjects are also covered. The journal is the primary place where crystallographic computer program information is published.

Crystallography Journals Online is available from journals.iucr.org

Imaging of strain and lattice orientation by quick scanning X-ray microscopy combined with three-dimensional reciprocal space mapping

Gilbert André Chahine,^{a*} Marie-Ingrid Richard,^{b,a} Roberto Arturo Homs-Regojo,^a Thu Nhi Tran-Caliste,^a Dina Carbone,^a Vincent Louis Robert Jaques,^a Raphael Grifone,^a Peter Boesecke,^a Jens Katzer,^c Ioan Costina,^c Hamid Djazouli,^a Thomas Schroeder^c and Tobias Urs Schüllli^a^aESRF, 6 rue Jules Horowitz, Grenoble 38000, France, ^bAix-Marseille Université, CNRS, IM2NP UMR 7334, Marseille Cedex 20, 13397, France, and ^cInnovations for High Performance Microelectronics, Frankfurt, Germany. Correspondence e-mail: gilbert.chahine@esrf.fr

Numerous imaging methods have been developed over recent years in order to study materials at the nanoscale. Within this context, scanning X-ray diffraction microscopy has become a routine technique, giving access to structural properties with sub-micrometre resolution. This article presents an optimized technique and an associated software package which have been implemented at the ID01 beamline (ESRF, Grenoble). A structural scanning probe microscope with intriguing imaging qualities is obtained. The technique consists in a two-dimensional quick continuous mapping with sub-micrometre resolution of a sample at a given reciprocal space position. These real space maps are made by continuously moving the sample while recording scattering images with a fast two-dimensional detector for every point along a rocking curve. Five-dimensional data sets are then produced, consisting of millions of detector images. The images are processed by the user-friendly X-ray strain orientation calculation software (*XSOCs*), which has been developed at ID01 for automatic analysis. It separates tilt and strain and generates two-dimensional maps of these parameters. At spatial resolutions of typically 200–800 nm, this quick imaging technique achieves strain sensitivity below $\Delta a/a = 10^{-5}$ and a resolution of tilt variations down to 10^{-3}° over a field of view of $100 \times 100 \mu\text{m}$.

© 2014 International Union of Crystallography

1. Introduction

The effects of strain and crystalline orientation dramatically change the performance of nanotechnological devices (Diaz *et al.*, 2009; Liu *et al.*, 2007; Falub *et al.*, 2013). Efficient characterization methods are thus required. Scanning probe microscopy methods are widely used for the characterization of nanomaterials, *e.g.* atomic force microscopy, transmission electron microscopy or scanning electron microscopy (SEM). In contrast, scanning X-ray diffraction microscopy (SXDM) is not limited to the study of the surface of structures but is a non-invasive technique sensitive to the lattice parameter in a probed volume (Evans *et al.*, 2012). It has allowed for the study of individual nanostructures (Mocuta *et al.*, 2008) and the resolution of the local microstructure of heterogeneous materials (Riekel *et al.*, 2000). As it utilizes X-rays, it can be used for the study of embedded structures as well as for *in situ* experiments (such as high temperature, pressure, electric or magnetic fields *etc.*) (Boscherini, 2008).

In this work we concentrate on the scanning probe techniques used in the diffraction condition and show that a significant optimization in data recording speed and online data

treatment can yield a scanning probe technique with unique capabilities at probing velocities comparable to those of established scanning probe microscopes. The spatial resolution is in this case limited by the size of the X-ray beam. However, the information about interatomic distances accessible by diffraction together with the available spatial resolution with focused beams render microdiffraction a highly interesting tool, able to image structural parameters of a crystalline sample. This scanning probe technique yields information at two length scales. The beam size defines the real space resolution of the scanning probe, while the beam divergence defines the resolution in reciprocal space and hence the interatomic distances and lattice orientations. The focal spot size S and the beam convergence 2α are correlated by the diffraction limit:

$$S = \lambda / (2 \sin \alpha). \quad (1)$$

The ultimate theoretical resolution limit is thus set by the wavelength λ . In reality the minimum reachable spot size S is, however, often limited by the source size and the required working distance in a diffraction experiment, which defines

the maximum demagnification ratio that can be obtained. On the other hand, the typical working regime of the method relies on the photon yield of the X-ray source, the scattering power of the sample, and the efficiency of the focusing optics and the detector. Under the conditions described in this work, the typical working regime corresponds to X-ray wavelengths of 0.1–0.2 nm, equating to the photon energy regime of 6.2–12.4 keV.

Assuming sufficient flexibility of the experimental setup and depending on the resolution requirements of the sample to be probed, the compromise between beam size and divergence can be made accordingly. The ultimate beam size limit is then often imposed by the source size and the required working distance between optics and sample. These parameters define the ratio at which the source can be de-magnified and thus the source image defines the focal spot. As compared to spectro-microscopic applications, where the smallest beam sizes can be supplied, diffraction with small beams often encounters the limit imposed by the working distance required for angular movements or by the required angular resolution of the beam.

In §2 of this article, we present the essential parameters of the improved scanning X-ray diffraction microscopy technique (quick mapping, K-Map) at ID01 and the resolution limits for these parameters. In §3, we present the test sample and the experimental setup. In §4, we present *XSOCS* and discuss the data results of the test sample before the conclusion in §5.

2. K-Map at ID01

2.1. Scanning X-ray diffraction microscopy at ID01

When aiming to study individual nanostructures with focused X-ray beams, a few basic experimental difficulties arise. The first is the structure localization. For this, SXDM offers a real space mapping of the sample that facilitates the localization of nanostructures. The second difficulty is related to the scanning time. Common beamline control programs, *e.g.* *SPEC* (Certified Scientific Software, Cambridge, MA, USA) at the ESRF, offer a variety of basic scan modes that are implemented in the software as step scans, *i.e.* sequences of distinct motor positioning and photon counting. The total time required for each step may be defined as $t = t_c + t_h$ where t_c is the exposure time, which is in most experiments determined by the required counting statistics and thus by the intensity diffracted by the sample. t_h is a holding and settling time, which includes data transfer and connection between the control program, the motors and the detectors. In addition, a lot of time can be dedicated to sending all of the data to the control program for saving. In this basic step-scan mode, t_h is of the order of 1 s per frame at ID01 when two-dimensional detectors are used. It is clear that even for very short exposure times t_c , the total time t required for each step can never become shorter than the settling time t_h .

With such bright sources as third-generation synchrotrons, the exposure time t_c required for acceptable counting statistics can be of the order of milliseconds in the case of thin films or

nanomaterials like the ones considered in this work (it may be even shorter for bulk materials). This is several orders of magnitude smaller than the settling time t_h in a basic step-scan mode. Using internal buffering available with photon counting pixel detectors, the framing time (exposure + readout) can be shorter than 1 ms. The weak point of the step-scan mode is thus clearly the positioning time of the hardware and software.

Getting round this issue considerably reduces the measurement time and thus allows users to perform many more measurements during an experiment. The K-Map developed at ID01 consists in reducing the overhead t_h as much as possible by parallelizing positioning, exposure and data handling. This allows fast quasi-continuous two-dimensional mapping.

For example, a two-dimensional real space map of $100 \times 100 \mu\text{m}$ making 500 nm spatial intervals (40 000 frames) with an exposure time of 10 ms per frame requires 11.2 h in step-scan mode. On the other hand, using the new continuous scanning mode, the same map can be obtained in less than 7 min (for $t_h = 1$ ms). The SXDM measurement time is significantly reduced, allowing fast localization of nanostructures. Moreover, three-dimensional reciprocal space maps requiring a rocking scan at every point become feasible. For example, in basic step-scan mode, making a spatial map at each angle of a 20-point rocking curve would require more than 9 d of measurement. Using the continuous scan mode, the complete five-dimensional data set can be recorded in less than 2.5 h. This is a very significant gain in time (two orders of magnitude) and is a prerequisite for the application of this method for the registration and exploitation of five-dimensional data. Apart from the limited availability of beam time, this reduction in measurement time is of practical importance: in the case where all data are to be assembled into a set of three-dimensional reciprocal space maps for each scan point, drifts of the beam, of the sample or of the diffractometer, estimated to be around $1 \mu\text{m}$ per day, would be detrimental. The shorter the total cycle time, the less time for drifts. Either the produced scanning probe images can be presented as the spatial distribution of diffracted intensity during one two-dimensional scan, or they may be generated on the basis of a reciprocal space analysis for every illuminated spot. Using a two-dimensional X-ray detector and repeating a two-dimensional real space scan at every point on a rocking curve, a three-dimensional reciprocal space map is recorded for every point of the scanned area. This quick mapping leads to five-dimensional data sets that allow for the unambiguous determination of the crystalline parameters of the sample: lattice strain and lattice orientation. At data rates of a few gigabytes per minute, the bottleneck for this type of scanning probe technique is the data treatment, especially to achieve real time visualization. Within this framework, a new software package, *XSOCS*, is developed to manage the five-dimensional data set, generating two-dimensional real space maps of strain and tilt distributions.

In the following section the K-Map principle is presented, together with its advantages and its potential, going far beyond the simple localization of a single nanostructure.

2.2. Quick mapping

K-Map has to meet the challenges of combining high-speed continuous motion of the positioning system with a precise and continuous readout together with high-frequency image recording and a trigger management that allows correlation of recorded diffraction images with positions in real space. The main components of this system are a pixel detector (MAXIPIX; Ponchut *et al.*, 2011), a piezo scanning stage (P-563 PIMars XYZ Piezo System, PI GmbH and Co.), and a hardware module that synchronizes the detector and the scanning stage. The parameters of the scanning sequence must be defined as usual in the control program (*SPEC* V6.00.03), and then the acquisition cycle is started on the fly. The raw data are buffered, compressed and automatically saved.

A multipurpose unit for synchronization sequencing and triggering (MUSST) card (<http://www.esrf.eu/Instrumentation/DetectorsAndElectronics/musst>), developed at the ESRF, ensures more efficient operation of the SXDM by generating trigger patterns synchronized with external events. In practice, a *SPEC* command is written by the operator, which includes the two-dimensional scanning range, the number of points per two-dimensional map and the counting time per point.

Then *SPEC* sends the scan spatial function (Figs. 1*b* and 1*c*) to the (x , y , z) (Fig. 1*a*) fast piezoelectric sample stage controller and prepares the two-dimensional photon detector to take instructions from the MUSST (steps 1.1 and 1.2 in Fig. 1). The scan parameters entered by the operator are sent to the MUSST card (Fig. 1, step 1.3), which sends triggering signals to the piezo stage (Fig. 1, step 2). Two motors of the piezoelectric stage can be scanned at a time. For a spatial scan defined by a *SPEC* command, *e.g.* from x_1 to x_2 with n_x steps and from y_1 to y_2 with n_y steps, and a counting time t_c , the first motor (here along x) moves across the whole scanning range

(trace from x_1 to x_2) before returning quickly (retracing) to the initial position (Fig. 1*b*). Then the second motor (here along y) moves one step further (Fig. 1*c*). This procedure is repeated until the second motor reaches its final position y_2 . The piezo stage sends a signal (step 3*a*) to the MUSST card (Fig. 1*d*, filled triangles), which generates a sequence of gate pulses for the detector (Fig. 1*e*, step 4) to take an image at each pulse (Fig. 1*f*). During the scan, the time and piezo motor positions are stored (step 3*b*) in the MUSST. For each image, integrated intensities over different regions of interest (ROIs) (see, for instance, the white squares in Fig. 1*f*) are stored in the detector controller. At the end of the scan, the data registered by the MUSST (time, position) and the detector controller (ROIs) are sent back to *SPEC* (Fig. 1, step 5) where they are merged into a 'specfile'.

With this setup, the previous controlling software (*SPEC*) of the detector and the piezo stage is replaced by a hardware controlling system (MUSST) (Fig. 1, Step 1.3), eliminating consequently the holding time t_h and reducing considerably the SXDM time. The images collected by the detector during the K-Map can be saved in the detector controller (step 6) in the ESRF data format (EDF).

3. Test sample and experimental setup

A test experiment was carried out at the ID01 beamline of the ESRF. We studied a 40 nm $\text{Si}_{0.8}\text{Ge}_{0.2}$ layer grown on an Si(001) substrate prepared at IHP in Frankfurt (Oder), Germany. Parts of the $\text{Si}_{0.8}\text{Ge}_{0.2}$ layer were removed with a focused ion beam (FIB) to draw the ESRF logo (inset Fig. 2*b*).

A Maxipix fast readout photon counting (frame rates of up to 300 Hz full frame) detector of 516×516 pixels and $55 \mu\text{m}$ pixel size was used, along with a scanning piezoelectric stage from PI. This setup has a stroke of $100 \mu\text{m}$ along x , y and z with an encoder resolution of about 1 nm (Fig. 3).

A monochromatic beam of 6.6 keV was focused by a tungsten fresnel zone plate (FZP) of $270 \mu\text{m}$ diameter and 80 nm outermost zone width, which leads to a focal distance of 11 cm. A $55 \mu\text{m}$ central beam stop (BS) was fixed right before the FZP (Fig. 3). A $50 \mu\text{m}$ molybdenum order sorting aperture (OSA) was mounted downstream of the FZP (Fig. 3) in order to remove higher diffraction orders. To optimize the resolution/flux compromise the zone plate was only illuminated by rectangular slits of 0.25 mm (h) \times 0.1 mm (v). The horizontal (h) and vertical (v) beam sizes with this setup are typically 350 nm (h) \times 200 nm (v), respectively, at a beam divergence (convergence) of about 0.1° (h) \times 0.05° (v) with an intensity of a few $10^9 \text{ photons s}^{-1}$. The sample was

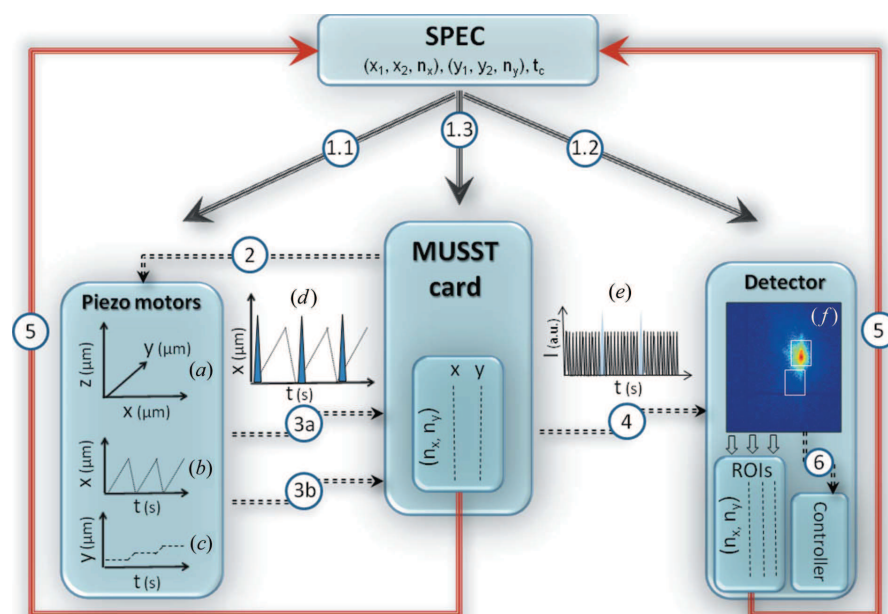


Figure 1
K-Map organizational structure.

mounted on the piezoelectric stage at the focal point of the FZP. The MAXIPIX detector was placed at a distance of 441 mm downstream of the sample. A microscope was used to observe the sample from the top and therefore allow for accurate sample positioning at the center of rotation of the goniometer.

Two radial scans (Fig. 2*b*) were performed around the 004 Si and $\text{Si}_{0.8}\text{Ge}_{0.2}$ Bragg reflections on an unstructured area and at the center of the ESRF logo (see labels 1 and 2 in Fig. 2*b*, respectively) to determine the exact position of the Si Bragg peak and to characterize the $\text{Si}_{0.8}\text{Ge}_{0.2}$ layer. Outside the ion milled area, a broad peak is observed around $Q = 4.5581 \text{ \AA}^{-1}$,

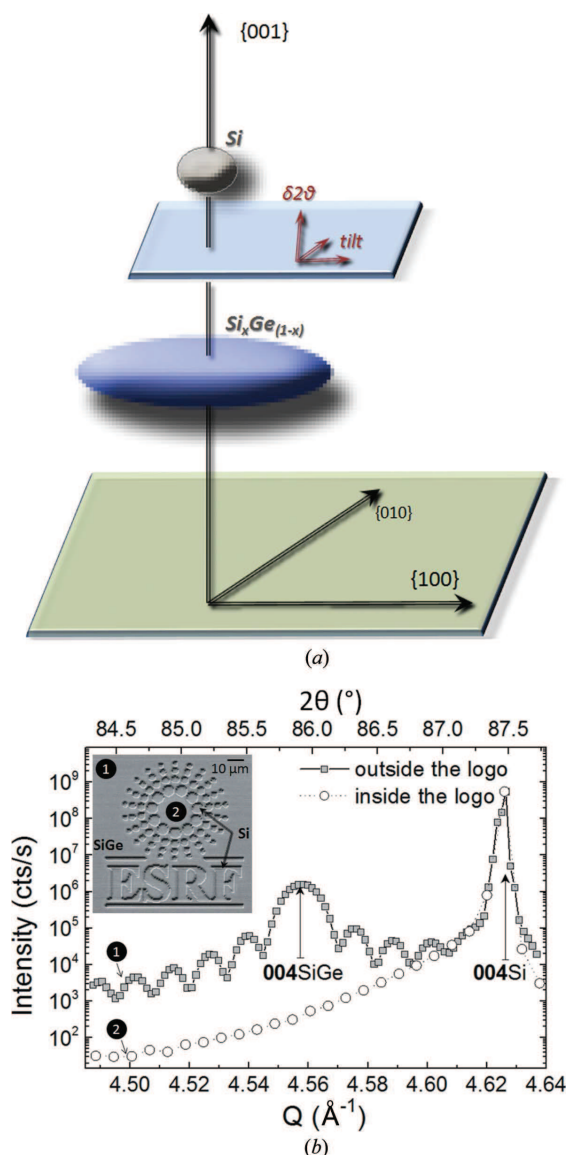


Figure 2

(*a*) Diagram of the three-dimensional reciprocal space volume near the Si 004 Bragg reflection and the diffraction signatures of $\text{Si}_{0.8}\text{Ge}_{0.2}$ (large ellipsoid). (*b*) θ – 2θ scans around the 004 Si and $\text{Si}_{0.8}\text{Ge}_{0.2}$ Bragg reflections outside and inside the structured ESRF logo. Inset: SEM image of the sample; the $\text{Si}_{0.8}\text{Ge}_{0.2}$ is present on the surface of the sample except inside the structures where it was locally removed, uncovering the buried Si.

related to the Ge layer. Thickness fringes from the $\text{Si}_{0.8}\text{Ge}_{0.2}$ thin film are clearly observed (Fig. 2*b*). They correspond to a film thickness of 40 nm. Inside the logo, no 004 $\text{Si}_{0.8}\text{Ge}_{0.2}$ peak is measured, despite the presence of an $\text{Si}_{0.8}\text{Ge}_{0.2}$ layer observed by scanning electron microscopy [see inset of Fig. 2(*b*)]. This implies that the $\text{Si}_{0.8}\text{Ge}_{0.2}$ layer inside the logo has been amorphized during the FIB process. At higher 2θ angles, a sharper and more intense peak appears at $Q = 4.6259 \text{ \AA}^{-1}$, which corresponds to the 004 Si substrate peak.

K-Map measurements were performed in the vicinity of the 004 Si Bragg reflection. The resulting two-dimensional maps are shown and discussed in the following.

In the micro XRD measurements, the determination of the Bragg peak position and shape in reciprocal space (Fig. 2*a*) is essential for retrieving all information related to strain and/or tilts in the structure. This information can only be accessed by recording a three-dimensional reciprocal space map of the investigated structure. In this way, all the components of the scattering vector \mathbf{Q} can be determined. The parameters that need to be extracted and represented as a function of their spatial distribution are (1) the length of the scattering vector $|\mathbf{Q}|$ and (2) its angular deviation from an orientation defined as ‘normal orientation’ in order to separate lattice deformation from lattice rotation. This latter value is a two-dimensional parameter generally referred to as lattice tilt.

For this purpose, a sample area of $100 \times 100 \mu\text{m}$ was K-Mapped, taking diffraction images with the two-dimensional MAXIPIX detector every 500 nm for different incidence angles ($42.8 < \omega < 43.088^\circ$) with steps of 0.018° , thus generating three-dimensional reciprocal space maps at each position on the sample. The K-Map measurement ends up with five-dimensional data to process and analyze: two dimensions for real space positions x and y , one for the incidence angle ω , and two for the detector scattering angles defined by 2θ and ν (taken with respect to the center of the detector, see Fig. 3). For our measurement, 17 (x, y) maps were recorded (for 17 incidence angles), leading to 907 256 two-dimensional

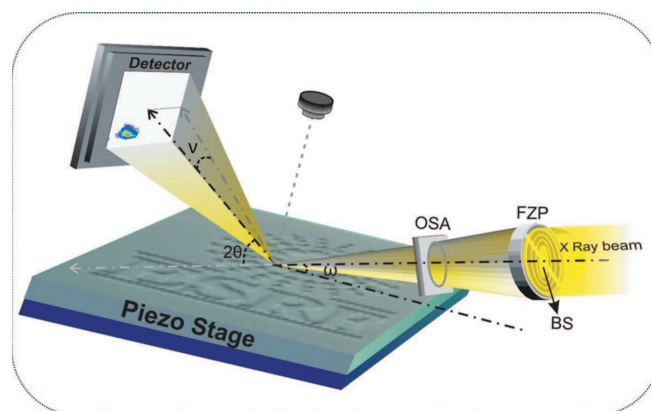


Figure 3

Schematic overview of the experimental setup in co-planar diffraction geometry. The X-ray beam is focused using an FZP. The incidence angle ω and the scattering angle 2θ are shown. ν denotes the deviation angle of the signal from the coplanar geometry. A microscope is positioned above the sample.

detector files, corresponding to a data volume of about 1 TB recorded in about 3 h.

Note that, during the retracing process, the MAXIPIX detector keeps recording and saving images at fixed frequency. Therefore, in this experiment, more images than the requested number (here, $17 \times 200 \times 200 = 680\,000$ images) are recorded.

With a data flow that can easily be in the 10 TB per day range, the data reduction (compression before or after processing) as well as the processing and online analysis represent another bottleneck of this method. The most important information is not necessarily included in the spatial variation of the diffracted intensity at a certain reciprocal space position, which can still be extracted fairly easily during or right after the measurement. The information about tilts and strain of the sample (particularly important in the case of thin films or monolithic semiconductor devices) is obtained by analyzing the Bragg peak displacements in reciprocal space at each position of the sample. The extraction of this information is a lengthy procedure, especially because it requires a composition of the three-dimensional reciprocal space maps associated with each position of the sample. These have then to be analyzed and fitted in order to be evaluated. It is thus clear that for a full analysis of the three-dimensional reciprocal space maps a highly efficient automatic data processing is mandatory.

XSOCS responds to this demand. It offers the opportunity to get preliminary results during the experiment, giving the user the opportunity to modify the measurement strategy. This is of particular importance for the application of such fast scanning methods to *operando* studies at high temperatures or in gas or liquid environments.

4. X-ray strain orientation calculation software

The *XSOCS* software (<https://sourceforge.net/projects/xsocs/files/>) is written in the Python script language. For an easy and simple use of *XSOCS*, a graphical interface has been developed using the PyGTK library. Its installation is possible on all major platforms (Windows, Mac and Linux/Unix). It works at two levels: (1) selecting the proper set of data for the analysis by removing the retracing effects and (2) offering complete analysis of strain and tilt by fitting the Bragg peak in reciprocal space.

4.1. Qualitative analysis of microstructured samples with two-dimensional intensity distribution maps

On the first level, *XSOCS* reads the specfile in which all motor positions (x , y , z , ω , 2θ and ν), the names of the recorded images and the defined ROIs are stored. During retracing (see part 2), images taken by the detector are not

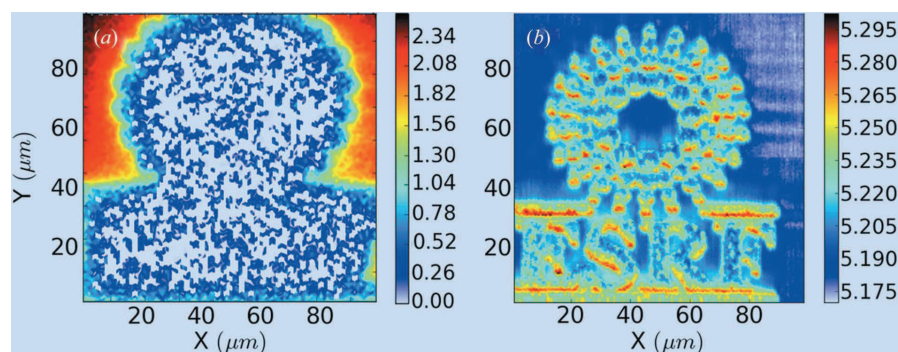


Figure 4

x - y meshes of the integrated intensity of the detector, (a) keeping the values collected during retracing and (b) removing them using the *XSOCS* package ($\omega = 42.89^\circ$, close to the 004 Si reflection).

meaningful and have to be removed (see Fig. 4). Then, *XSOCS* goes through all registered counters and reads the corresponding motor positions, ROIs and image numbers, storing afterwards all values or strings in .npy three-dimensional matrices. The first two dimensions of these matrices correspond to the real space positions x and y of the beam on the sample, while the third dimension corresponds to the ω values. At this level of data treatment, the user can plot one-dimensional lines or two-dimensional meshes of the integrated intensity over different ROIs of the detector for a given ω value. A three-dimensional isosurface of an integrated intensity can also be displayed as a function of the two scanning directions and the incident angle.

Plotting the intensity distribution in real space for selected regions in reciprocal space is a first qualitative analysis which can be achieved quickly as it is economical in computing time (no conversion from pixels to angular coordinates and three-dimensional fitting in every pixel are required). Doing so already allows a striking comparison with the information supplied by scanning electron microscopy. As shown in Fig. 5(a), the 004 $\text{Si}_{0.8}\text{Ge}_{0.2}$ layer, located inside the logo, has been damaged and amorphized during the FIB process as the integrated intensity decreases drastically as soon as the beam hits the structured area [see region labeled 2 in Fig. 2(b)]. Outside the logo [see region labeled 1 in Fig. 2(b)], the 004 $\text{Si}_{0.8}\text{Ge}_{0.2}$ layer remains crystalline, giving high-intensity values in the corners of Fig. 5(a). Although the structured sample surface is still clearly visible on the SEM image (inset, Fig. 2b), K-Map proves here to be highly sensitive to the sample crystallinity and allows detection of the structure quality (epitaxial, polycrystalline, amorphous *etc.*) inside nanometric volumes defined by the beam. Defects like stacking faults (Richard *et al.*, 2007; Jacques *et al.*, 2013) or strain heterogeneities can even be revealed by this technique. The ESRF logo appears (Fig. 5b) when making a two-dimensional map of the integrated intensity in the vicinity of the 004 Si Bragg reflections.

The nonhomogeneous distribution of the integrated intensity over the scanned region indicates the presence of structural inhomogeneities, *e.g.* crystalline mosaicity or strain distribution.

4.2. Fitting of the three-dimensional peak positions in reciprocal space – complete analysis of strain and tilt

For a precise calculation and decoupling of strain and lattice tilt, the *XSOCS* program converts the scattering angles into reciprocal space coordinates and generates a three-dimensional reciprocal space map at each sample position. To achieve the required precision in terms of strain resolution, the origin of reciprocal space as well as the definition of the gridding (detector pixels per degree) is determined by the *XSOCS* package. First, the users record the pixel position corresponding to the reciprocal space origin by imaging the direct beam in the detector. The second calibration is made by loading three images of the direct beam for different values of the detector arm motors. For each ω value, each pixel of the detector is converted into detector angles and to its corresponding reciprocal space coordinates, which are coordinates of the scattering vector $\mathbf{Q} = \mathbf{k}_f - \mathbf{k}_i$, where \mathbf{k}_i is the wavevector of the incident X-ray beam and \mathbf{k}_f the wavevector of the

scattered beam towards a particular detector (pixel) position. This conversion is performed using the *xrayutilities* package (Kriegner *et al.*, 2013), which is written in Python with some performance-critical parts written internally in the C programming language. For each position (x, y) on the sample, *XSOCS* creates a three-dimensional reciprocal space volume along the reciprocal space coordinates (Q_x , Q_y and Q_z) as shown in Fig. 6. In this figure, the double peak is the shadow of the BS holder (tungsten wire) fixed on the FZP.

XSOCS performs numerical Gaussian peak fitting to locate the Q_x , Q_y and Q_z coordinates of the Bragg peak in the corresponding reciprocal dimension. In this experiment, the fitting was performed over 120 000 curves generating two-dimensional matrices for the scattering vector coordinates Q_x , Q_y and Q_z after 4 h of processing (see Figs. 7a–7c). In the present example of the specular 004 Si reflection, the length of the scattering vector mainly depends on the variation of its z component Q_z .

The strain ε_{hkl} is related to the variation of the lattice parameter a_{Si} and consequently to the variation of the d_{hkl} spacing of the atomic planes. It can be retrieved using equation (2) for each position in real space:

$$\varepsilon_{hkl} = \frac{d_{hkl,\text{meas}} - d_{hkl,\text{ref}}}{d_{hkl,\text{ref}}}, \quad (2)$$

where $d_{hkl,\text{ref}}$ is the reference d spacing corresponding to the unstrained lattice and $d_{hkl,\text{meas}}$ results from the measurement as

$$d_{hkl} = \frac{2\pi}{|\mathbf{Q}|} = \frac{2\pi}{(Q_x^2 + Q_y^2 + Q_z^2)^{1/2}}. \quad (3)$$

The determination of the strain ε_{hkl} then only depends on the total length of the scattering vector \mathbf{Q} . Fig. 7(d) displays the out-of-plane strain, ε_{004} , as a function of sample position. The value of $d_{hkl,\text{ref}}$ was taken to be equal to the experimental Si d spacing d_{004} measured far away from the ESRF logo. The two-dimensional plot of the strain distribution (Fig. 7d) shows that the Si layer underneath the $\text{Si}_{0.8}\text{Ge}_{0.2}$ structured logo is slightly strained ($<0.0015\%$) as a result of the FIB process.

In Figs. 7(a) and 7(b), the shift from zero of the scattering vector components Q_x and Q_y indicates possible tilts of the {001} atomic planes with respect to the sample surface normal. A proper characterization and calculation of the tilt angles may be done by *XSOCS*, which uses the following relation:

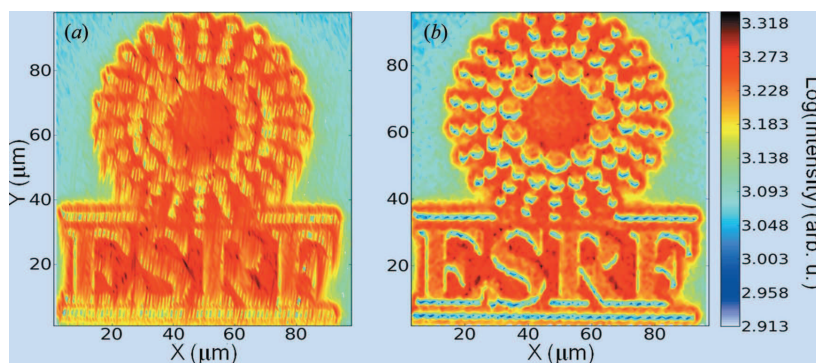


Figure 5
(a) Integrated intensity at the 004 $\text{Si}_{0.8}\text{Ge}_{0.2}$ Bragg position at $\omega = 42.920^\circ$. (b) Two-dimensional plot of the integrated intensity at $\omega = 42.998^\circ$ in the region of the diffuse scattering of the 004 Si Bragg peak.

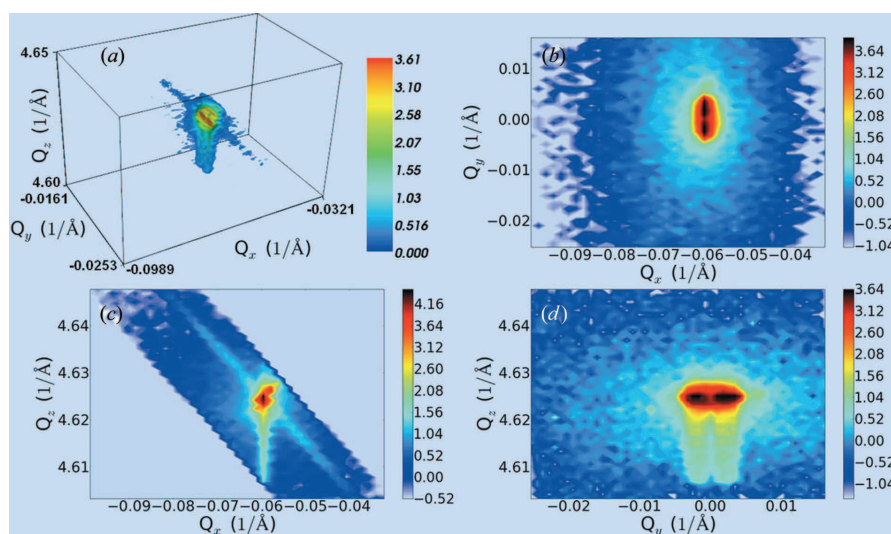


Figure 6
(a) Three-dimensional representation of the Si 004 Bragg peak for a given real space position ($x = 25.5 \mu\text{m}$, $y = 25.5 \mu\text{m}$) on the sample. Two-dimensional cuts of the Bragg peak in reciprocal space as a function of Q_x and Q_y (b), Q_x and Q_z (c), and Q_y and Q_z (d).

$$\text{tilt}(^{\circ}) = (180/\pi) \arccos[Q_z/(Q_x^2 + Q_y^2 + Q_z^2)^{1/2}]. \quad (4)$$

Fig. 8(a) shows that the ESRF logo can be resolved by plotting the two-dimensional tilt distribution. Therefore, strain is not the only structural effect induced by the FIB process. The Si {001} planes show slight tilts up to 0.0024° under the structured $\text{Si}_{0.8}\text{Ge}_{0.2}$ area. Fig. 8(b) shows that, under the structured $\text{Si}_{0.8}\text{Ge}_{0.2}$, the FIB process does not induce any preferential orientation.

The low strain and tilt values measured by the K-Map show in two-dimensional plots that lattice variations of the order of $\Delta a/a < 10^{-5}$ still produce a significant contrast. The heterogeneous materials (Etzelstorfer *et al.*, 2014) that are used in most microelectronic devices (Evans *et al.*, 2012; Kozłowski *et*

al., 2011; Capellini *et al.*, 2013) present weak structural variations that affect their performance. Accessing these faint variations is therefore of high importance.

5. Conclusion

Having the three-dimensional reciprocal Bragg peak information, a precise study of crystalline structures and composition can be obtained, as well as tilts, strain distribution or even thickness fluctuations of thin films. We described measurements that could be applied to typical samples like epitaxial films or any kind of crystalline structures with preferential orientation and a local variation/deviation from it. These are representative for the majority of electronic devices

or functional materials in a wider sense.

The K-Map presents an optimized kind of scanning probe microscopy capable of accessing in a quick way structural properties without any surface or morphological limitations. The method itself, however, is not limited to such samples but can be applied to any crystalline object, even polycrystalline thin films. During a K-Map measurement with a spatial resolution of 200–300 nm, a two-dimensional real space scan is performed over several incidence angles, and corresponding images are recorded on a two-dimensional detector. After this measurement, one ends up with five-dimensional data to analyze and to process. A complementary software package, *XSOCS*, offers a quick and easy way to handle five-dimensional sets of data and large numbers of files that are challenging in terms of both data storage management and data treatment. With the almost complete suppression of the dead time and the availability of detectors that can operate in the kHz regime, the scanning speed is defined by the statistical limit which at a given spatial resolution is ultimately limited by the brilliance of the source. The technique will definitely benefit from the multiple upgrade projects currently being carried out or planned at several third-generation sources and is likely to become a routine analysis technique for processed semiconductor devices.

References

- Boscherini, F. (2008). *Characterization of Semiconductor Heterostructures and Nanostructures*, edited by C. Lamberti, ch. 9, pp. 289–331. Amsterdam: Elsevier.

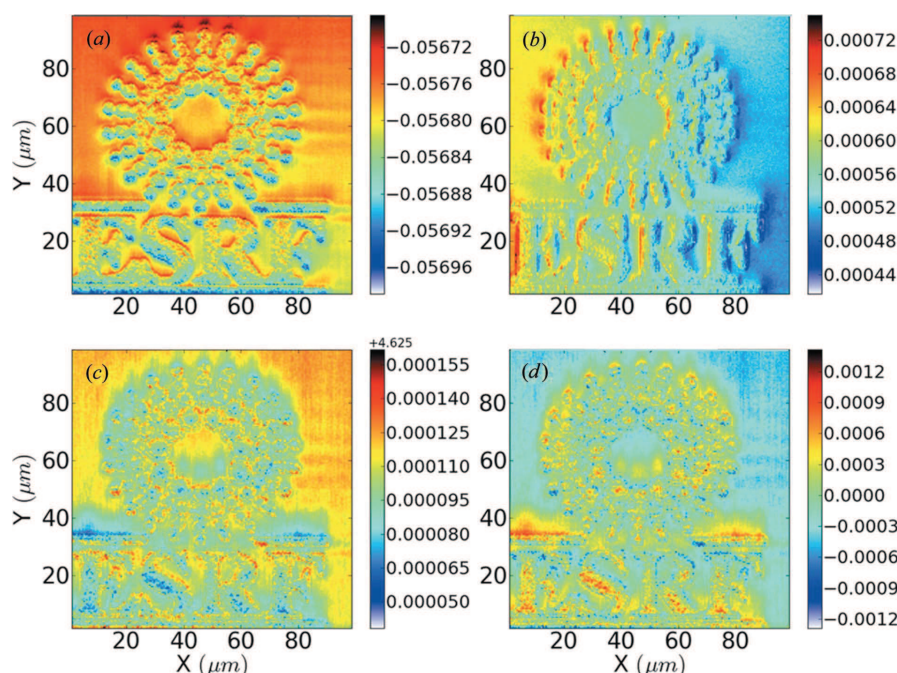


Figure 7 Scattering vector coordinates (a) Q_x , (b) Q_y and (c) Q_z , and (d) out-of-plane strain as a function of real beam position on the sample.

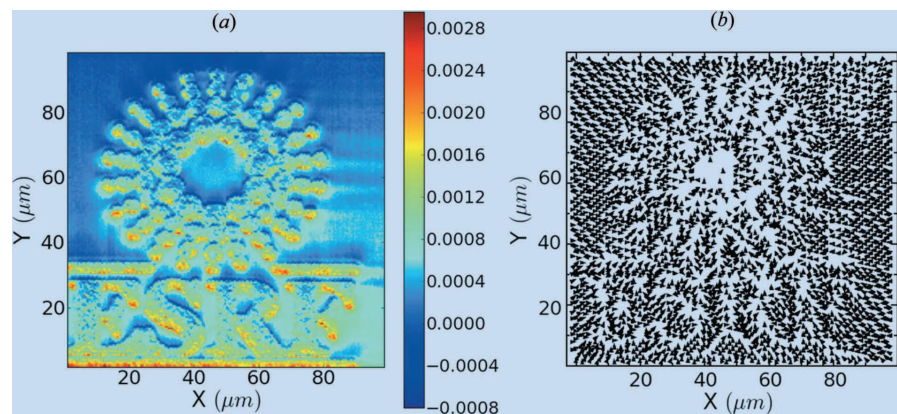


Figure 8 (a) Two-dimensional map distribution of the tilt magnitude ($^{\circ}$) and (b) directional representation (arrows) of tilted {001} atomic planes with respect to the sample surface normal.

- Capellini, G. *et al.* (2013). *J. Appl. Phys.* **113**, 013513.
- Diaz, A., Mocuta, C., Stangl, J., Mandal, B., David, C., Vila-Comamala, J., Chamard, V., Metzger, T. H. & Bauer, G. (2009). *Phys. Rev. B*, **79**, 125324.
- Etzelstorfer, T., Süess, M. J., Schiefler, G. L., Jacques, V. L. R., Carbone, D., Chrastina, D., Isella, G., Spolenak, R., Stangl, J., Sigg, H. & Diaz, A. (2014). *J. Synchrotron Rad.* **21**, 111–118.
- Evans, P. G., Savage, D. E., Prance, J. R., Simmons, C. B., Lagally, M. G., Coppersmith, S. N., Eriksson, M. A. & Schülly, T. U. (2012). *Adv. Mater.* **24**, 5217–5221.
- Falub, C. V., Meduna, M., Chrastina, D., Isa, F., Marzegalli, A., Kreiliger, T., Taboada, A. G., Isella, G., Miglio, L., Dommann, A. & von Känel, H. (2013). *Sci. Rep.* **3**, 2276.
- Jacques, V. L. R., Carbone, D., Ghisleni, R. & Thilly, L. (2013). *Phys. Rev. Lett.* **111**, 065503.
- Kozłowski, G., Zaumseil, P., Schubert, M. A., Yamamoto, Y., Bauer, J., Matejova, J., Schulli, T., Tillack, B. & Schroeder, T. (2011). *Appl. Phys. Lett.* **99**, 141901.
- Kriegner, D., Wintersberger, E. & Stangl, J. (2013). *J. Appl. Cryst.* **46**, 1162–1170.
- Liu, J., Sun, X., Pan, D., Wang, X., Kimerling, L. C., Koch, T. L. & Michel, J. (2007). *Opt. Express*, **15**, 11272–11277.
- Mocuta, C., Stangl, J., Mundboth, K., Metzger, T. H., Bauer, G., Vartanyants, I. A., Schmidbauer, M. & Boeck, T. (2008). *Phys. Rev. B*, **77**, 245425.
- Ponchut, C., Rigal, J. M., Clément, J., Papillon, E., Homs, A. & Petitdemange, S. (2011). *J. Instrum.* **6**, C01069.
- Richard, M. I., Metzger, T. H., Holý, V. & Nordlund, K. (2007). *Phys. Rev. Lett.* **99**, 225504.
- Riekkel, C., Burghammer, M. & Müller, M. (2000). *J. Appl. Cryst.* **33**, 421–423.